ACS OMEGA

http://pubs.acs.org/journal/acsodf

Article

Impact of Y_2O_3 Nanosheets on the Microstructural Characteristics of Alq_3 Prepared via the Co-precipitation Route for Enhancement of Photodiode Performance

Miad Ali Siddiq,* Manar Sopaih, and Elsayed Elgazzar

Cite This: ACS Omega 2023, 8, 24883−24892

Read Online

ACCESS | Metrics & More | Article Recommendations | Supporting Information

ABSTRACT: In the present study, tris-(8-hydroxyquinoline) aluminum (Alq_3) and tris-(8-hydroxyquinoline) aluminum/yttrium oxide Alq_3/Y_2O_3 were synthesized by a facile chemical route. The crystal structure, surface morphological nature, and particle size were identified by X-ray diffraction (XRD), scanning electron microscopy (SEM), and transmission electron microscopy (TEM) micrographs. Ag/Alq_3/p-Si/Al and Ag/Alq_3:Y_2O_3/p-Si/Al diodes were fabricated by the thermal evaporation technique and the electrical characteristics were evaluated from the $I-V$ plots in dark and under illumination intensity. Thermionic emission theory, Cheung−Cheung, and Nord model have been applied to define the main electronic parameters like series resistance (R_s), barrier height (ϕ_b), and ideality factor (n). The hybrid Ag/Alq_3:Y_2O_3/p-Si/Al diode revealed a nonideal behavior with high shunt resistance R_{sh} and good photocurrent sensitivity. The $C/G-V$ analysis indicated that both C and G are strongly affected by the presence of trapped charge carriers at the interface states. The obtained results indicated that R_s was decreased whereas the carrier concentration (N_a) was increased by loading Y_2O_3 nanosheets.

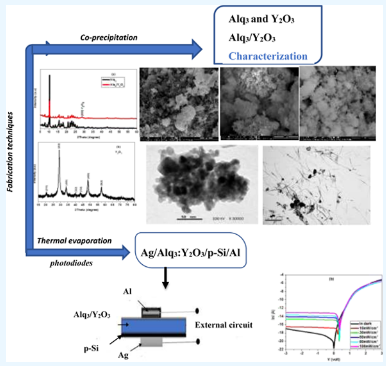

1. INTRODUCTION

The increase of pollution and spread of global warming due to industrial development and excessive use of traditional energy such as coal, oil, and nuclear power represent a great danger to human life and environment. Nowadays, the scientific community is working on using novel strategies for fabricating alternative, renewable, and highly efficient energy systems. Nanotechnology-based nanomaterials were demonstrated as the best solution. Hybrid composites consisting of metal-organics, organometallics, and organic/metal oxides have gained great attention during the recent decade. These compounds are flexible, available, light-weight, environmentally friendly, and easily prepared at low temperatures.[1,2] Recently, metal-phthalocyanine (MPc) and tris(8-hydroxyquinoline) metals (Mq_3) have been utilized as electron-transporting materials for manufacturing optical sensors and organic solar cells (OSCs). Tris-(8-hydroxyquinoline) aluminum (Alq_3) molecules with wide optical absorption, versatile electro-luminescence and photoluminescence properties, weak Van der Waals force, and various crystalline states (α, β, ε, δ, γ) have been employed in fabricating organic light-emitting diodes (OLEDs). In a recent study, Sevgili et al. have investigated the morphological and optical properties of aluminum 8-hydroxyquinoline microbelts and microdots for improvement of the photodiode performance.[3] However, Mq_3 compounds have some drawbacks like low charge carrier mobility and weak electrical conductivity. In general, Mq_3 molecules have the ability to interact with a wide range of materials comprising metals, metal oxide nanoparticles (NPs), and carbonaceous materials, carbon nanotubes (CNTs), graphene, and graphene oxide (GO). Therefore, integration of the Alq_3 framework with different nanomaterials will produce new composites with promising characteristics that combine inorganic−organic ligands.[4,5] In this context, Sharma et al. have studied the influence of the DCJTB organic dye on the electronic and spectroscopic features of Alq_3 for modifying OLEDs' behavior.[6] Furthermore, rare earth metal oxide semiconductors (REMOSs) such as cerium oxide (CeO_2), lanthanum(III) oxide (la_2O_3), lutetium(III) oxide (Lu_2O_3), and yttrium(III) oxide (Y_2O_3) have displayed great importance in numerous technological applications thanks to their photostability, redox capabilities, and electromagnetic aspects.[7] In particular, Y_2O_3 of nanoscale particle size, good luminescence, and excellent physical−chemical stability has been used for removing organic pollutants, biological activities, supercapacitor implementations, and biomedical and live-cell imaging. Moreover, Y_2O_3 NPs can react with the organic framework, creating surface organometallic fragments for advancement of the photoelectrical activity in light emitters

Received: February 13, 2023
Accepted: June 7, 2023
Published: July 3, 2023

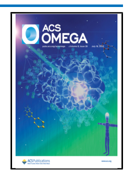

and photovoltaics. Because of the large ionic radius of yttrium (Y^{3+}) 1.02 Å, doping of Y_2O_3 inside the host material causes the structure to deteriorate, the crystallite size to reduce, and, consequently, the surface area to increase.[7,8] It is worthy to note that tuning of the physical properties of Alq_3 is strongly dependent on its quantum size confinement, which is executed by Y_2O_3 nanosheet integration. In a previous study, Arif Kösemen has reported the electrochemically grown yttrium-doped ZnO NR P3HT:PCBM as an electron selective layer for promoting the organic solar cell efficacy.[9] There are several common chemical approaches used for preparing the nanomaterials, such as spray pyrolysis, precipitation, hydrothermal treatment, and sol−gel. Among them, the chemical co-precipitation method has provided a great contribution to modern science owing to its friendly environment, modular, and easy scaling up. The co-precipitation procedure is quick, controllable, and straightforward. It is easy to produce high-quality nanostructures with specific shape, composition, and particle size by monitoring the annealing temperature, medium pH, precursor ratio, dopant type, and contents.[10,11] In the current investigation, hybrid Alq_3/Y_2O_3 was synthesized by a scalable chemical approach. X-ray diffraction (XRD), scanning electron microscopy (SEM), and transmission electron microscopy (TEM) techniques were used to investigate the microstructure characteristics of the nanoparticles. The findings have proved the significant impact of Y_2O_3 nanosheet contents on modulation of the structural-morphological properties of Alq_3 for enhancement of the photodiode efficiency.

2. EXPERIMENTAL SECTION

2.1. Chemicals and Reagents. 8-Hydroxyquinoline (C_9H_7NO), aluminum nitrate nonahydrate [$Al(NO_3)_3\cdot 9H_2O$], sodium hydroxide (NaOH), yttrium(III) chloride hexahydrate ($YCl_3\cdot 6H_2O$), and p-type silicon (p-Si). All reagents were purchased from Merck and Alfa Easer Company.

2.2. Preparation of Alq_3, Y_2O_3, and Hybrid Alq_3:Y_2O_3 Nanoparticles. The Alq_3 nanopowder was prepared from the reaction of 8-hydroxyquinoline and aluminum nitrate, as demonstrated in Scheme 1. Firstly, solution A (HQ solution) was prepared by dissolving 6.97 g of 8-hydroxyquinoline in 100 mL of absolute ethanol. Besides, solution B was prepared by dissolving 6.00 g of $Al(NO_3)_3\cdot 9H_2O$ in 100 mL of deionized water. Consequently, solution A was added to solution B with full stirring at a constant speed of 900 rpm for 25 min. After that, 6.75 g of NaOH was dissolved in 50 mL of double-distilled water (3.375 mol L^{-1}) for 30 min, then added drop by drop to the mixture until the pH reaction medium was 6. The whole mixture was refluxed for 1 h, then left on stirring for 24 h at room temperature. The resulting precipitate was filtered off under vacuum, washed with distilled water, and then dried in a furnace at 150 °C overnight. The rare earth metal oxide Y_2O_3 NPs were prepared by dissolving 3.20 g of $YCl_3\cdot 6H_2O$ in 40 mL of deionized water. Then, 25 mL of NaOH (1.27 g of dissolved in 30 mL of deionized water, 1.058 mol L^{-1}) was carefully added dropwise to the yttrium chloride solution with continuous stirring for another 3 h. Subsequently, a homogenous white precipitate was formed at pH ∼ 9. The resulting powder was separated by filter paper, washed many times using deionized water, dried in an oven at 80 °C for 12 h, and eventually annealed at 420 °C in air for 2 h. The hybrid Alq_3/Y_2O_3 was prepared by dissolving 0.50 g of Alq_3 in 25 mL of absolute ethanol and 0.05 g of Y_2O_3 in 20 mL of deionized water/ethanol solution in the ratio 1:1. Thereafter, the Y_2O_3 solution was added drop by drop to the Alq_3 solution under stirring at room temperature. The mixture was heat-treated in a microwave oven under a power level of 420 W for 30 min, then centrifuged. The resulting nanocomposite was washed and left for drying in a furnace at 80 °C for 12 h.

Scheme 1. Synthesis of Alq_3

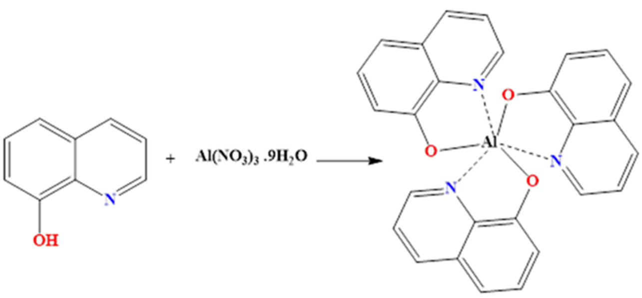

2.3. Fabrication and Characterization of the Fabricated Photodiodes. Alq_3 and Alq_3/Y_2O_3 solutions were separately deposited onto the surface of p-type silicon using a spin coater technique. Before deposition, the silicon wafers were etched using dilute hydrofluoric acid (HF), then cleaned with double-distilled water and acetone bath in the ratio 3:1 each, and finally washed several times using deionized water. The silver (Ag) metal top contact was evaporated, giving a diode contact area of 3.20×10^{-2} cm^2, via the thermal evaporation technique. The electrical characterization was analyzed using a programmable (Keithley 6517b) electronic device. The photocurrent sensitivity was examined using a solar simulator and the light intensity was measured using a solar power meter (TM-206). In the frequency range from 10 kHz to 1 MHz, a computerized HIOKI 3531-Hi-tester LCR meter was employed for $C/G-V$ and R_s-V analysis. The X-ray diffraction (XRD) was carried out using a Cu Kα radiation source (λ = 1.5405) in a Rigaku D/max-2400 XRD spectrometer to identify the crystal structure of the nanoparticles. Scanning electron microscopy (SEM; Helios Nanolab. 400) was performed to check the surface morphology. A JEOL (Model: JEM 1400) transmission electron microscope was utilized to visualize the shape, size, and particle distribution of the nanomaterials.

3. RESULTS AND DISCUSSION

3.1. Structural and Morphological Analysis. The X-ray diffraction was examined at room temperature to identify the phase and crystal structure of the synthesized nanoparticles with the 2θ angle ranging from 5 to 60°. The dominant diffraction peaks at 2θ = 09.835, 10.384, 13.668, 15.324, 18.054, 21.078, 22.044, and 24.062° are obvious. These reflection peaks are indexed to the pure phase of polymorphs Alq_3 according to the standard card (JCPDS 26-1550, Figure 1a). A peak related to Y_2O_3 was observed at 2θ = 28.900°; this peak clearly confirms the integration of the nanoparticles inside the host Alq_3 lattice.[12,13] Moreover, the crystal structure of Y_2O_3 was defined by the XRD pattern with the 2θ angle changing from 15 to 80°. The peaks located at 2θ = 20.443, 28.966, 33.657, 40.069, 43.510, 48.417, and 57.624° according to the reflection planes 211, 222, 400, 322, 134, 400, and 662 are ascribed to the cubic crystal structure of pure Y_2O_3 and coincide with the standard card (JCPDS file No. 83-0927).[14]

https://doi.org/10.1021/acsomega.3c00962
ACS Omega 2023, 8, 24883−24892

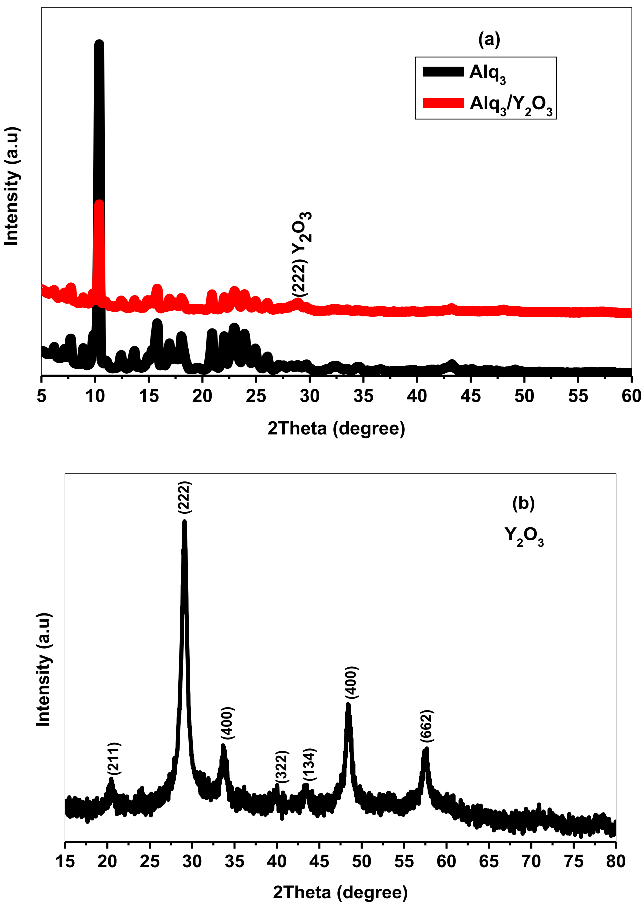

Figure 1. XRD pattern of (a) undoped and Y_2O_3-doped Alq_3 and (b) pure Y_2O_3 nanopowder.

As shown in Figure 1b, the polycrystalline Y_2O_3 has a broad diffraction peak attributed to the small crystalline size. Scherrer equation was applied to identify the crystallite size of Y_2O_3 by taking the full width at half maximum (FWHM) of the maximum diffraction peak (222)

$$D = \frac{K\lambda}{\beta \cos \theta} \tag{1}$$

β is the line broadening at FWHM, $k = 0.94$ is the shape factor, and λ is the wavelength of incident X-ray radiation (1.540 Å). The crystal size was calculated to be around ~12 nm; the nanoscale particle size plays an essential role in promoting the efficiency of the optical materials. Due to the particle size reduction, the density of the particles increases, leading to a large surface to volume area and accordingly, a high surface reactivity. With quantum confinement effect, more energy levels of electrons are generated, which significantly boost the chemical reactivity and the electrical conductivity of the nanoparticles.[14−16]

The morphological nature and average size of the nanoparticles were visualized from the SEM and TEM micrographs. Figure 2a shows the particles of Alq_3 in tiny granular shapes; the surface appears rough and not uniform.[15−17] The granular particles were decorated with the nanosheets and the Alq_3/Y_2O_3 NPs were observed to have high density, as depicted in Figure 2b. The SEM image in Figure 2c shows the particles of Y_2O_3 in a nanosheet-like structure; the surface is relatively smooth and uniform.[17,18] For further microstructure analysis, the TEM was examined to define the shape and particle size. Figure 2d describes the particles of Alq_3 in nanoscale; some of them are aggregated together with a mean size of ~40 nm. Figure 2e demonstrates the nanoparticles covered with thin sheets composing the nanocomposite Alq_3/Y_2O_3 with a small particle size of ~15 nm.[19,20] The size confinement is associated with the large surface area of the nanomaterial, which is useful in optoelectronics and photodetector devices.

3.2. Evaluation of the Photodiode Performance under Dark. The semilogarithmic current−voltage (I−V) plot of Alq_3/p-Si and hybrid Alq_3:Y_2O_3/p-Si diodes was investigated. Based on the thermionic emission (TE) theory, the transport mechanism is attributed to the discharge of majority of the carriers, in which the current of the Schottky barrier diode is associated with the applied voltage. As observed in Figure 3a, the photodiodes possess a good rectification behavior (RR) of 86 and 55 for Alq_3/p-Si and Alq_3:Y_2O_3/p-Si, respectively. According to the TE theory, the current of the metal-semiconductor junction depends on both the voltage and temperature from the relation

$$I = I_s \exp\left(\frac{q(V - IR)}{nKT}\right)\left[1 - \exp\left(-\frac{q(V - IR_s)}{KT}\right)\right] \tag{2}$$

The reverse saturation current I_s is given by

$$I_s = AA^*T^2 \exp\left(\frac{-q\phi_b}{kT}\right) \tag{3}$$

Here, V, q, K, A, A^*, and T are the applied voltage, electronic charge (1.6×10^{-19} C), Boltzmann constant (1.38×10^{-23} J K^{-1}), effective rectifying area, Richardson's constant (32 A cm^{-2} K^{-2}) for p-type silicon, and the absolute temperature (300 Kelvin), respectively.[21,22] At low voltage, I_s was calculated to have very low values, suggesting a little leakage current. The saturation current values were used to determine the barrier height ϕ_b from the following equation

$$\phi_b = \frac{kT}{q} \ln\left(\frac{AA^*T^2}{I_s}\right) \tag{4}$$

The ideality factor (n) is an important electronic parameter and can be expressed as

$$n = \frac{q}{kT}\frac{dV}{d\ln(I)} \tag{5}$$

The ideality factor was calculated to be greater than unity, exhibiting the nonideal behavior of the photodiodes. Many factors affect the ideality factor, making it higher than unity, like series resistance, inhomogeneity of the heterojunctions, forming an oxide layer, as well as the bad contact between the semiconductor and metal contacts. Furthermore, the series resistance R_s and shunt resistance R_{sh} were determined from the R_j−V graph, as illustrated in Figure 3b. The obtained electronic parameters are summarized in Table 1. The composite diode Alq_3:Y_2O_3/p-Si exhibited a low series resistance, small potential barrier, and high shunt resistance, attributed to the Y_2O_3 replacements and increase of the charge carrier transportation to metal contacts.[23−25]

To confirm the diode quality, Cheung−Cheung model was applied. In this approach, both n and R_s were identified using the relation

https://doi.org/10.1021/acsomega.3c00962
ACS Omega 2023, 8, 24883−24892

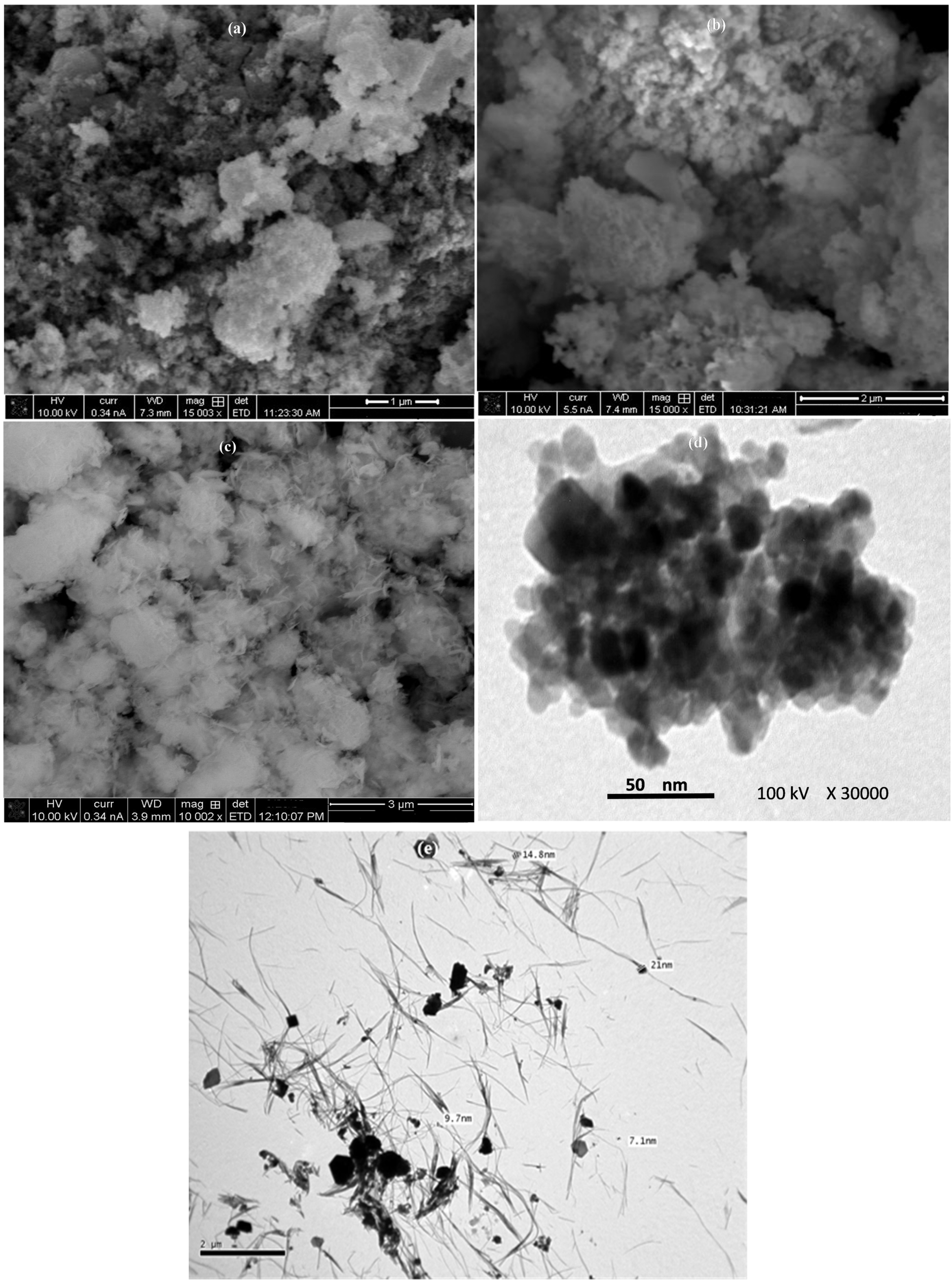

Figure 2. SEM micrographs of (a) Alq_3, (b) hybrid Alq_3/Y_2O_3, and (c) Y_2O_3 nanosheets, and the TEM images of (d) Alq_3 and (e) Alq_3/Y_2O_3.

$$\frac{dV}{d(\ln I)} = \frac{nkT}{q} + IR_s \tag{6}$$

From the plot of $dV/d(\ln I)$ against I in Figure 4a, R_s was determined from the slope of the straight part and n was obtained from the intercept $= nkT/q$. Further, ϕ_b was determined by the following relation

$$H(I) = V - \left(\frac{nkT}{q}\right)\ln\left(\frac{I}{AA^{*}T^{2}}\right) = n\phi_b + IR_s \tag{7}$$

From the $H(I)-I$ plot in Figure 4b, the slope provides R_s, while ϕ_b was calculated from the intercept $(n\phi_b)$. Nord function was applied to define R_s and ϕ_b again using the equation

$$F(V) = \frac{V}{\gamma} - \frac{kT}{q}\ln\left(\frac{I(V)}{AA^{*}T^{2}}\right) \tag{8}$$

γ is the first integer greater than the ideality factor. From the $F(V)$ vs. V graph in Figure 5, $F_o(V)$ was calculated to be 0.724 and 0.652 corresponding to V_o of 1.17 and 1.11 volt for the undoped and composite diode, respectively. These values were used to determine the barrier height from eq S1, Supporting Information, and R_s was calculated using eq S2, Supporting Information. It was observed from Table 1 that the results obtained from the TE theory and Cheung−Cheung model coincide with each other, whereas they are in deviation with the Nord model. This deviation is because Nord functions are suitable for the ideal diode, which could not be achieved in the current study. Also, this may be owing to the impact of the series resistance at higher voltages in the case of Nord model,

https://doi.org/10.1021/acsomega.3c00962
ACS Omega 2023, 8, 24883−24892

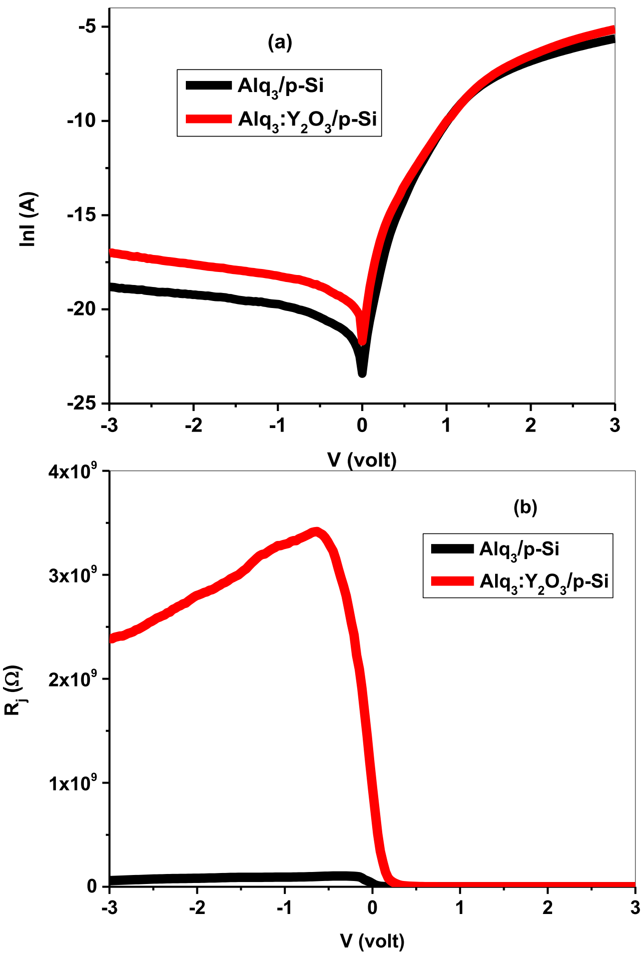

Figure 3. (a) (I–V) characteristics and (b) (R_j–V) plot of Alq_3/p-Si and Alq_3:Y_2O_3/p-Si diodes.

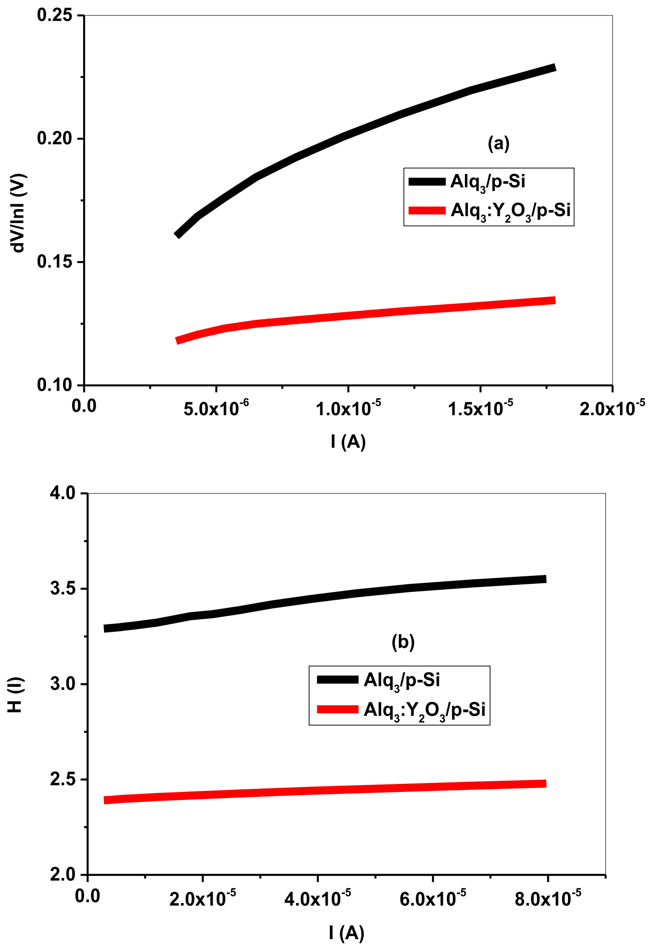

Figure 4. Cheung–Cheung plots of (a) $dV/d\ln I$ versus I and (b) $H(I)$ versus V plots of Alq_3/p-Si and Alq_3:Y_2O_3/p-Si diodes.

while the TE and Cheung models are applied at low voltages, 0 > V > 0.3.[25,26] The obtained results revealed the significant impact of the nanosheets on improvement of the surface area of the nanocomposite Alq_3/Y_2O_3, leading to create more excitons, which separated into free charge carriers (holes and electrons) at the interfacial layers.[25−27]

3.3. Influence of Illumination Intensity on the Photodiode Behavior. The photocurrent sensitivity of the fabricated diodes was investigated under different illumination conditions. As seen in Figure 6a, the photocurrent of the Alq_3/p-Si diode was increased from 5.83×10^{-10} A in the dark to 1.22×10^{-6} A under illumination intensity. However, the current of the hybrid Alq_3:Y_2O_3/p-Si diode was increased from 7.11×10^{-9} to 1.85×10^{-6} A, Figure 6b. When the light was incident on the diode, more charge carriers were generated, resulting in increase in the number of photoelectrons. The transient photocurrent was examined as shown in Figure 7a,b. With illumination, the current suddenly increased to a certain level and remained constant there as the maximum. After turning off, the current comes back to its initial state because of the presence of trapped charge carriers at the deep levels.[28,29] Furthermore, the photodiode conductivity dependence of the light intensity and trap centers' response was described according to the following equation

$$I_{Ph} = AP^m \tag{9}$$

Here, I_{Ph} is the photocurrent, A is a constant, P is the illumination intensity, and m is an exponent estimated from the slope of the relation $\ln I_{Ph}$–$\ln P$ in Figure 7c. The exponent m was 1.01 and 1.13 for Alq_3/p-Si and Alq_3:Y_2O_3/p-Si, respectively. The m values indicated that the trap centers inside the energy gap are responsible for enhancement of the photosensitivity.[29−31]

Table 1. Electronic Parameters of the Fabricated Diodes Estimated by Thermionic Emission Theory, Cheung Model, and Nord Function

	thermionic emission theory					Cheung–Cheung model				Nord function	
						[$dV/d\ln I$–I] plot		[$H(I)$–I] plot			
the photodiode	n	Φ_b (eV)	R_s (Ω)	$R_{sh} \times 10^8$ (Ω)	I_s (nA)	n	R_s (Ω)	Φ_b (eV)	R_s (Ω)	R_s (Ω)	Φ_b (eV)
Ag/Alq_3/p-Si/Al	1.88	0.690	4000	1.02	0.018	5.90	4691	0.624	3733	1313	1.28
Ag/Alq_3:Y_2O_3/p-Si/Al	1.65	0.642	2164	34.00	0.095	4.61	1064	0.520	1151	376	1.18

https://doi.org/10.1021/acsomega.3c00962
ACS Omega 2023, 8, 24883−24892

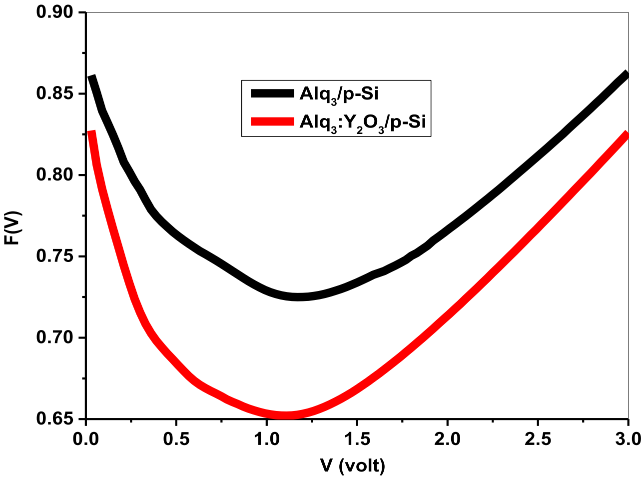

Figure 5. $F(V)-V$ curves of the fabricated diodes.

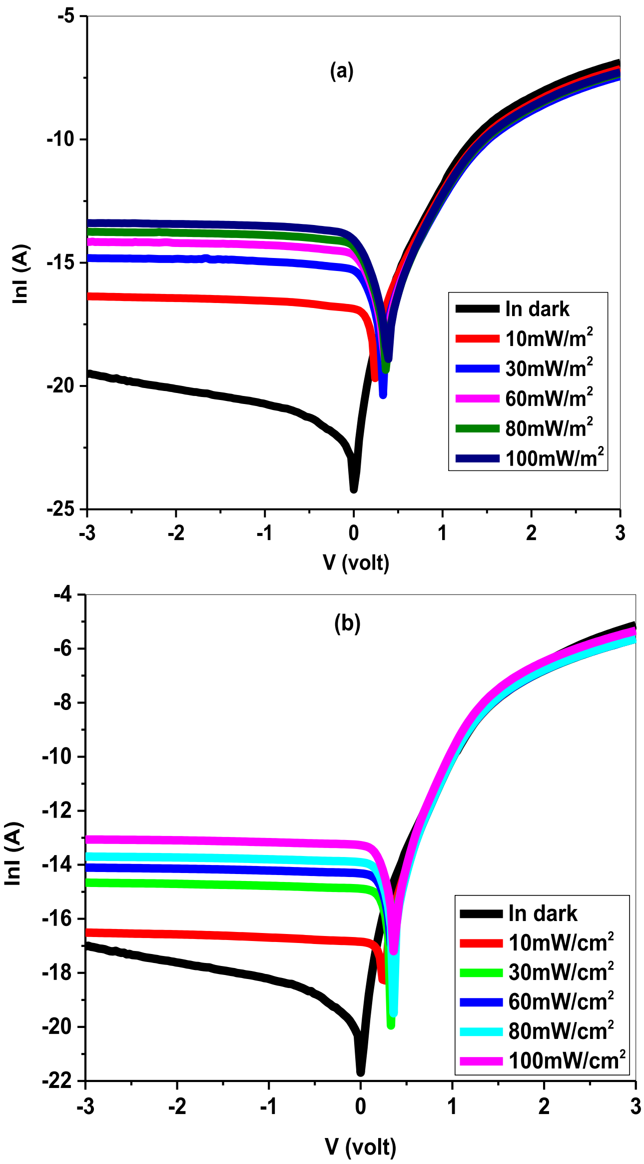

Figure 6. $I-V$ characteristic curve under different illumination intensities of (a) Alq$_3$/p-Si and (b) Alq$_3$:Y$_2$O$_3$/p-Si diodes.

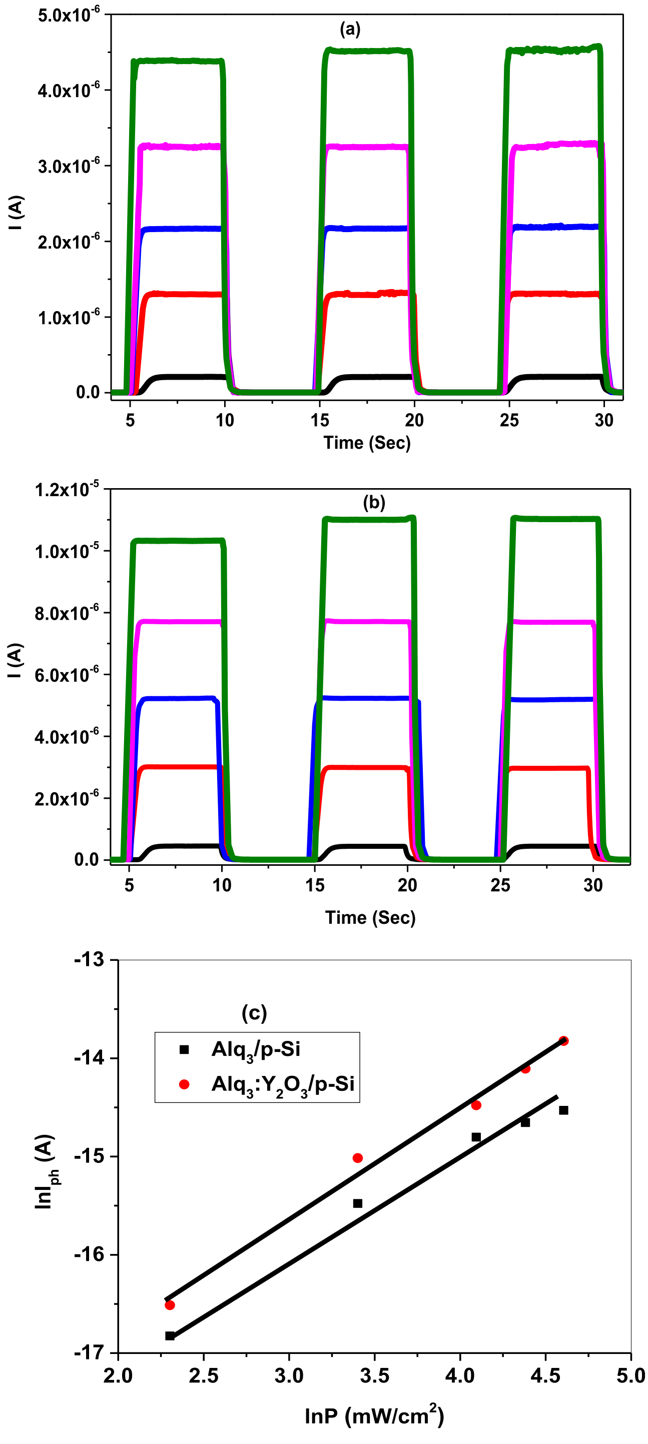

Figure 7. $I-T$ plots of (a) Alq$_3$/p-Si, (b) Alq$_3$:Y$_2$O$_3$/p-Si composite diode, and (c) phototransient current of the fabricated devices.

3.4. (*C/G–V*) and (*R$_s$–V*) Analysis. The measured C_p and corrected capacitance C_{adj} of the synthesized diodes were examined as a function of voltage and frequency. The C_p of Alq$_3$/p-Si diode has a characteristic peak in the reverse bias at −0.70 volt; this peak was decreased, shifted to higher voltage, and its width increased with frequency, Supporting Information (Figure S1). To study the impact of series resistance, the capacitance was corrected using eq S3 in the Supporting Information. The C_{adj} of Alq$_3$/p-Si diode was significantly decreased at low frequencies, attributed to the presence of trapped charge carriers at the interfacial layers of the

https://doi.org/10.1021/acsomega.3c00962
ACS Omega 2023, 8, 24883−24892

heterostructures that follow the alternating current signals (AC) at low values, Figure 8.[32,33] The C_p of the Alq_3:Y_2O_3/p-Si

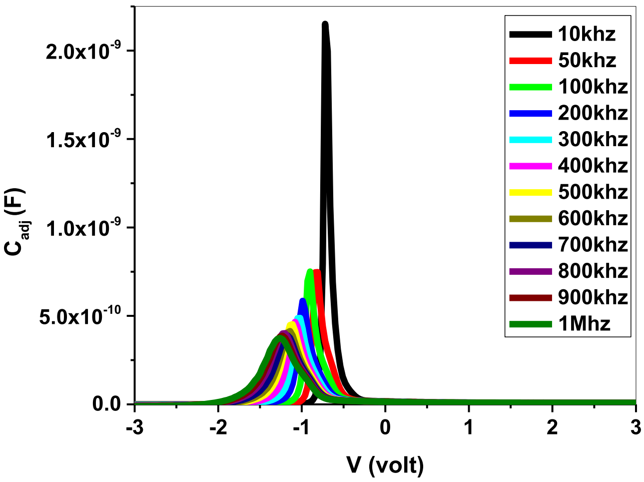

Figure 8. $C_{adj}-V$ characteristics of the Ag/Alq_3/p-Si/Al diode.

diode was slightly decreased with the applied frequencies, Supporting Information (Figure S2). As illustrated in Figure 9,

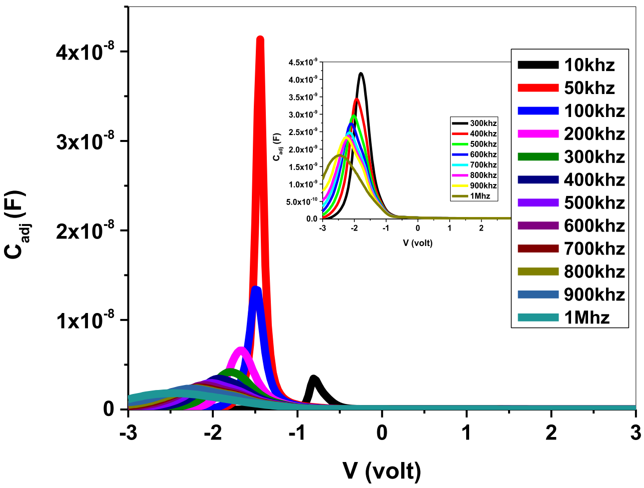

Figure 9. $C_{adj}-V$ characteristics of the Ag/Alq_3:Y_2O_3/p-Si/Al photodiode.

the C_{adj} of the hybrid diode was regularly decreased, broadened, and shifted to a higher reverse bias due to the presence of series resistance as well as the dopant Y_2O_3 concentration. The response of the interface states is strongly dependent on the dielectric relaxation frequency as well as the change in thermal emission rate of Alq_3. It is worthy to note that the charge carriers would follow the Ac signals when the frequency is less than the relaxation frequency. Herein, the nanosheets result in generating more free charge carriers at the interface states and hence, depletion region reduction.[34−36] The conductance-voltage (G_p-V) and corrected conductance-voltage ($G_{adj}-V$) were measured as a function of the frequency. The G_p of the Alq_3/p-Si diode was irregularly changed, without a specific behavior, as depicted in the Supporting Information (Figure S3). The diode conductance was corrected using eq S4 in the Supporting Information.[37,38] As illustrated in Figure 10, the G_{adj} of the Alq_3/p-Si diode was increased at frequencies greater than 300 kHz. There is no

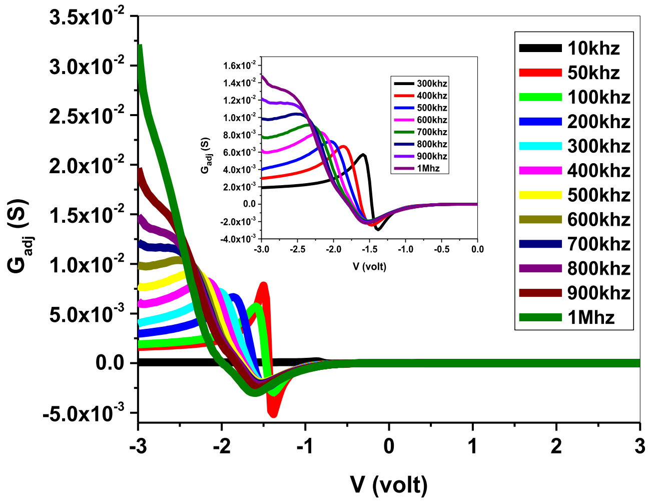

Figure 10. $G_{adj}-V$ characteristics of the Ag/Alq_3/p-Si/Al diode.

significant impact on the G_p of the hybrid diode Alq_3:Y_2O_3/p-Si as shown in Figure S4, Supporting Information. However, G_{adj} was regularly increased with the applied frequency associated with the Y_2O_3 support, Figure 11. On the other

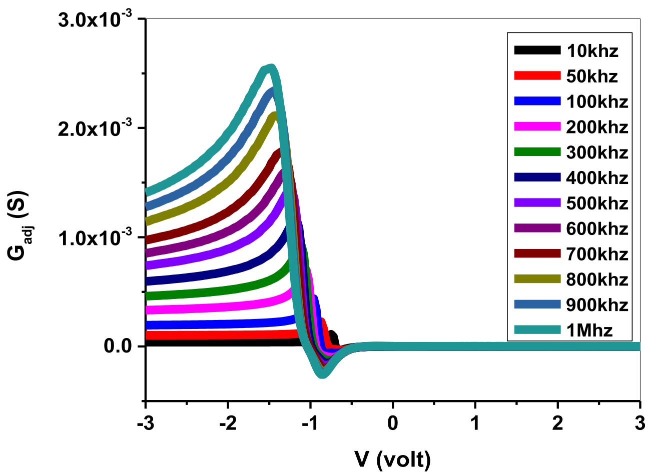

Figure 11. $G_{adj}-V$ characteristics of the Ag/Alq_3:Y_2O_3/p-Si/Al diode.

side, the series resistance R_s of the Ag/Alq_3/p-Si/Al photodiode was as shown in Figure 12. The magnitude of R_s at 0.1 and −0.7 volt was significantly decreased with increasing frequency owing to the high response of the trapped charge carriers to the ac signals causing more free carrier transportation.[39,40] The R_s of the Ag/Alq_3:Y_2O_3/p-Si/Al photodiode showed a similar behavior, as shown in Figure S5, Supporting Information.

Mott Schottky (M−S) method was utilized to define the acceptor atom concentration N_a and the built-in voltage V_{bi} at the interface states by the capacitance equation, eq S5 in the Supporting Information. According to M−S approach, the interfacial layers are formed at the edges of the diode device by doping. The barrier height ϕ_b was described by eq S6 in the Supporting Information. From the Mott Schottky ($1/C^2-V$) relation depicted in Figure 13, the slope of the straight line gives N_a and the intercept defines V_{bi}.[41,42] The value of N_a was used to calculate the barrier height from eq S6, in the Supporting Information. The values of N_a and ϕ_b are presented in Table 2. The $C-V$ analysis indicated that the hybrid diode

https://doi.org/10.1021/acsomega.3c00962
ACS Omega 2023, 8, 24883−24892

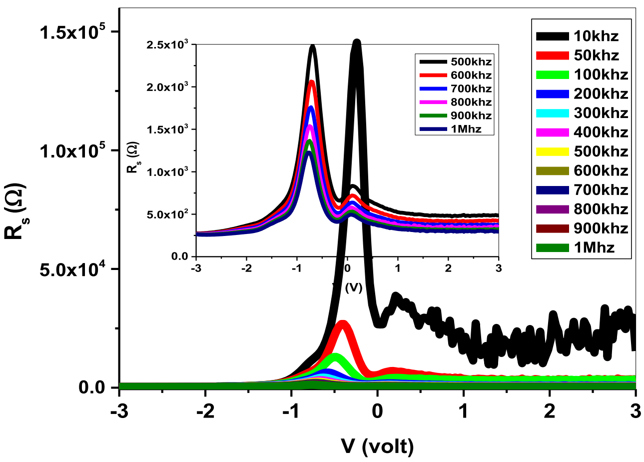

Figure 12. R_s−V plot of the Ag/Alq_3/p-Si/Al photodiode.

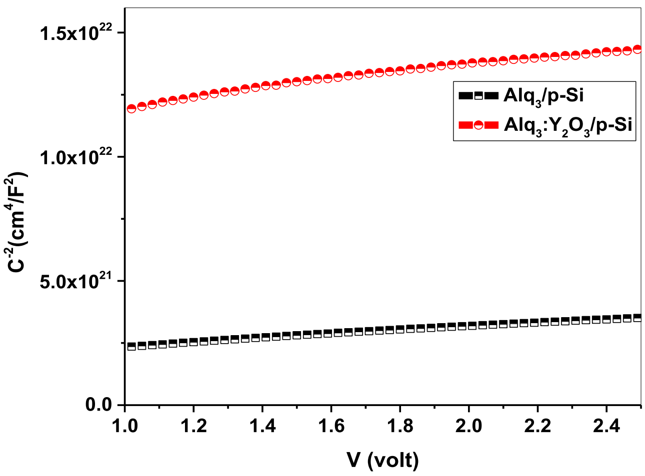

Figure 13. $1/C^2$ versus V plot of the fabricated photodiodes.

has a low potential barrier, small series resistance, and large charge carrier density.[43,44]

Table 2. Built-in Voltage (V_{bi}), Acceptor Concentration (N_a), and Barrier Height (Φ_b) Evaluated from the (C−V) Analysis

	(C−V) calculations		
photodiode	V_{bi} (V)	$N_a \times 10^{20}$ (cm^{-3})	Φ_b (eV)
Ag/Alq_3/p-Si/Al	−0.67	7.67	0.710
Ag/Alq_3:Y_2O_3/p-Si/Al	−0.50	73.46	0.616

4. CONCLUSIONS

The Alq_3 and Alq_3/Y_2O_3 nanomaterials were successfully prepared by the cost-effective co-precipitation approach. The structural-morphological analysis confirmed the modulation of the Alq_3 framework by the nanosheet dopants, showing that as the particle size of the nanocomposite Alq_3/Y_2O_3 decreased, its surface area was increased. The unique microstructure aspects enable the synthesized nanocomposite to be used for enhancement of the Ag/Alq_3:Y_2O_3/p-Si/Al performance. The main electronic parameters, comprising R_s, n, and ϕ_b, were calculated in the dark from the I−V graph by applying the thermionic emission, Cheung−Cheung, and Nord models. The hybrid diode displayed a low R_s and small ϕ_b, suggesting the easy electron transfer to the metal contacts. Under a light power impact, the photoconductivity was increased, anchored to the large number of photogenerated charge carriers. Additionally, the C/G−V measurements revealed that the hybrid diode Ag/Alq_3:Y_2O_3/p-Si/Al of high conductance and large charge carrier concentration resulted from the trapped centers' response to the AC signals as well as nanosheet integration.

■ ASSOCIATED CONTENT

Supporting Information

The Supporting Information is available free of charge at https://pubs.acs.org/doi/10.1021/acsomega.3c00962.

Data of Nord, capacitance and barrier height equations; in addition to, the C−V plot of Ag/Alq_3/p-Si/Al diode (Figure S1); C−V characteristics of Ag/Alq_3:Y_2O_3/p-Si/Al photodiode (Figure S2); G−V plot of Ag/Alq_3/p-Si/Al diode described (Figure S3); G−V characteristics of Ag/Alq_3:Y_2O_3/p-Si/Al diode (Figure S4), and the R_s−V plot of Ag/Alq_3:Y_2O_3/p-Si/Al diode (Figure S5) (PDF)

■ AUTHOR INFORMATION

Corresponding Author

Miad Ali Siddiq − *Department of Chemistry, University College in Samtah, Jazan University, Jazan 45142, Saudi Arabia;* orcid.org/0000-0002-4032-5462; Email: msiddiq@jazanu.edu.sa

Authors

Manar Sopaih − *Chemistry Department, Faculty of Science, Suez Canal University, Ismailia 41522, Egypt*

Elsayed Elgazzar − *Department of Physics, Faculty of Science, Suez Canal University, Ismailia 41522, Egypt;* orcid.org/0009-0009-9857-972X

Complete contact information is available at: https://pubs.acs.org/10.1021/acsomega.3c00962

Notes

The authors declare no competing financial interest.

■ ACKNOWLEDGMENTS

The authors would like to thank both Jazan University, Jazan, Saudi Arabia and Suez Canal University, Ismailia, Egypt for facilitating and supporting the research collaboration.

■ REFERENCES

(1) Saeed, A.; Salah, N.; Alshahrie, A.; Baghdadi, N.; Gauthaman, K.; Memic, A. Tunable fabrication of rice-like nanostructures aggregated into flowers of Alq_3 with negligible photo-degradation for potential biomedical applications. *Mater. Chem. Phys.* **2021**, *259*, No. 124080.

(2) Samantaray, M. K.; Mishra, S. K.; Saidi, A.; Basset, J.-M. Surface organometallic chemistry: A sustainable approach in modern catalysis. *J. Organomet. Chem.* **2021**, *945*, No. 121864.

(3) Sevgili, O.; Canlı, S.; Akman, F.; Orak, I.; Karabulut, A.; Yıldırım, N. Characterization of aluminum 8-hydroxyquinoline microbelts and microdots, and photodiode applications. *J. Phys. Chem. Solids* **2020**, *136*, No. 109128.

(4) Abdullahi, S.; Aydarous, A.; Salah, N. Fabrication of Alq_3/PMMA nanocomposite sheet and its potential applications as radiation dosimeter. *J. Lumin.* **2022**, *242*, No. 118588.

(5) Dasi, G.; Lavanya, T.; Suneetha, S.; Vijayakumar, S.; Shim, J.-J.; Thangaraju, K. Raman and X-ray photoelectron spectroscopic investigation of solution processed Alq_3/ZnO hybrid thin films. *Spectrochim. Acta, Part A* **2022**, *265*, No. 120377.

(6) Sharma, G.; Hashmi, S. Z.; Kumar, U.; Kattayat, S.; Ayaz Ahmad, M.; Kumar, S.; Dalela, S.; Alvi, P. A. Optical and electronic characteristics of ITO/NPB/Alq_3:DCJTB/Alq_3/Ag heterostructure based organic light emitting diode. *Optik* **2020**, *223*, No. 165572.

(7) Richard, D.; Rentería, M.; Carbonari, A.; Romero, M.; Faccio, R. Preparation of In-doped Y_2O_3 ceramics through a sol-gel process: Effects on the structural and electronic properties. *Ceram. Int.* **2020**, *46*, 16088−16095.

(8) Zhao, H.; Xia, J.; Yin, D.; Luo, M.; Yan, C.; Du, Y. Rare earth incorporated electrode materials for advanced energy storage. *Coord. Chem. Rev.* **2019**, *390*, 32−49.

(9) Kösemen, A. Electrochemical growth of Y doped ZnO nanorods for use in inverted type organic solar cells as electron transport layer. *Mater. Res. Express* **2019**, *6*, No. 095024.

(10) Rajakumar, G.; Mao, L.; Bao, T.; Wen, W.; Wang, S.; Gomathi, T.; Gnanasundaram, N.; Rebezov, M.; Shariati, M. A.; Chung, I.-M.; Thiruvengadam, M.; Zhang, X. Yttrium Oxide Nanoparticle Synthesis: An Overview of Methods of Preparation and Biomedical Applications. *Appl. Sci.* **2021**, *11*, 2172.

(11) Patil, A. S.; Patil, A. V.; Dighavkar, C. G.; Adole, V. A.; Tupe, U. J. Synthesis techniques and applications of rare earth metal oxides semiconductors: A review. *Chem. Phys. Lett.* **2022**, *796*, No. 139555.

(12) Darwish, A. A. A.; Qashou, S. I.; Alenezy, A. G. K.; Al Garni, S. E.; Alatawi, N. S.; Alsharif, M. A.; Hamdalla, T. A.; Alharbi, F. M.; Abdulrhman; Alsharari, M. Preparation and characterizations of Erbium(III)-Tris(8-hydroxyquinolinato) nanostructured films for possible use in gas sensor. *Sens. Actuators, A* **2022**, *340*, No. 113550.

(13) Abdullahi, S.; Aydarous, A.; Salah, N. Effects of X-ray irradiation on the structural and optical properties of microcrystalline Alq_3 powder and its potential dosimetry application. *Radiat. Phys. Chem.* **2021**, *188*, No. 109656.

(14) Prasannakumar, J. B.; Vidya, Y. S.; Anantharaju, K. S.; Ramgopal, G.; Nagabhushana, H.; Sharma, S. C.; Daruka Prasad, B.; Prashantha, S. C.; Basavaraj, R. B.; Rajanaik, H.; Lingaraju, K.; Prabhakara, K. R.; Nagaswarupa, H. P. Bio-mediated route for the synthesis of shape tunable Y_2O_3:Tb^{3+} nanoparticles: Photoluminescence and antibacterial properties. *Spectrochim. Acta, Part A* **2015**, *151*, 131−140.

(15) Raj, V.; Kamaraj, P.; Sridharan, M.; Arockiaselvi, J. Green synthesis, characterization of yttrium oxide, stannous oxide, yttrium doped tin oxide and tin doped yttrium oxide nanoparticles and their biological activities. *Mater. Today: Proc.* **2021**, *36*, 920−922.

(16) Kaszewski, J.; Witkowski, B. S.; Wachnicki, L.; Przybylinska, H.; Kozankiewicz, B.; Mijowska, E.; Godlewski, M. Reduction of Tb^{4+} ions in luminescent Y_2O_3:Tb nanorods prepared by microwave hydrothermal method. *J. Rare Earths* **2016**, *34*, 774−781.

(17) Mohan, A.; Sahayaraj, M.; Velusamy, J.; et al. Room temperature investigations on altered properties of Alq_3 in a facile thermal evaporated Alq_3/In/Alq_3 thin-film structures. *Opt. Mater.* **2022**, *126*, No. 112184.

(18) Kannan, S. K.; Sundrarajan, M. Biosynthesis of Yttrium oxide nanoparticles using *Acalypha indica* leaf extract. *Bull. Mater. Sci.* **2015**, *38*, 945−950.

(19) Reddy, L. P.; Rajprakash, H. G.; Ravikiran, Y. T. Synthesis of Yttrium Trioxide (Y_2O_3) Nanoparticles and Investigations of Its Humidity Sensing Properties. In *AIP Conference Proceedings*; AIP Publishing LLC, 2019; Vol. *2142*.

(20) Nath, S. G.; Anila, E. I. Photoluminescence studies of non-toxic monoclinic yttrium oxide quantum dots synthesized at low temperature for live cell imaging applications. *Ceram. Int.* **2023**, *49*, 13200−13207.

(21) Alzahrani, H.; Sulaiman, K.; Mahmoud, A. Y.; Bahabry, R. R. Study of organic visible-blind photodetector based on Alq_3:NPD blend for application in near-ultraviolet detection. *Opt. Mater.* **2020**, *110*, No. 110490.

(22) Thapaswini, P. P.; Padma, R.; Balaram, N.; Bindu, B.; Rajagopal, V. Reddy, Modification of electrical properties of Au/n-type InP Schottky diode with a high-k$Ba_{0.6}Sr_{0.4}TiO_3$interlayer. *Superlattice Microstruct.* **2016**, *93*, 82−91.

(23) Sadakata, A.; Osada, K.; Taguchi, D.; Yamamoto, T.; Fukuzawa, M.; Manaka, T.; Iwamoto, M. Probing interfacial charge accumulation in ITO/a-NPD/$Alq_{3/}$Al diodes under two electrolumin-escence operational modes by electric-field induced optical second-harmonic generation. *J. Appl. Phys.* **2012**, *112*, No. 083723.

(24) Osama, R.; Morsy, M.; Al-Kamel, A. N.; Mahmoudd, E. A.; Ashery, A.; El-Sayed, A. Stimulating photodiode characteristics of hybrid ZnPc-MWCNTs. *J. Alloys Compd.* **2021**, *891*, No. 161783.

(25) de Barros Silveira Lacerda, G. R.; dos Santos Junior, G. A.; Rocco, M. L. M.; Lavall, R. L.; Matencio, T.; Calado, H. D. R. Development of a new hybrid CNT-TEPA@poly(3,4-ethylenedioxythiophene-co-3-(pyrrol-1-methyl)pyridine) for application as electrode active material in supercapacitors. *Polymer* **2020**, *194*, No. 122368.

(26) Karabulut, A.; Yıldız, D. E.; Kose, D. A.; Yıldırım, M. Photosensing performances of heterojunctions-based photodiodes with novel complex interlayers. *Mater. Sci. Semicond. Process.* **2022**, *146*, No. 106647.

(27) Gürgenç, E.; Dıkıcı, A.; Aslan, F. Investigation of structural, electrical and photoresponse properties of composite based Al/NiO:CdO/p-Si/Al photodiodes. *Phys. B* **2022**, *639*, No. 413981.

(28) Elgazzar, E. Improvement the efficacy of Al/CuPc/n-Si/Al Schottky diode based on strong light absorption and high photocarriers response. *Mater. Res. Express* **2020**, *7*, No. 095102.

(29) Aslan, F.; Esen, H.; Yakuphanoglu, F. The effect of coumarin addition on the electrical characteristics of Al/Coumarin: CdO/p-Si/Al photodiode prepared by drop casting technique. *Optik* **2019**, *197*, No. 163203.

(30) Dayan, O.; Imer, A. G.; Tercan, M.; Dere, A.; Al-Sehemi, A. G.; Al-Ghamdi, A. A.; Yakuphanoglu, F. Dye sensitized solar cell-based optoelectronic device using novel [Ru $(L_1)(L_2)(NCS)_2$] complex. *J. Mol. Struct.* **2021**, *1238*, No. 130464.

(31) Gozeh, B. A.; Karabulut, A.; Ismael, C. B.; Saleh, S. I.; Yakuphanoglu, F. Zn-doped CdO effects on the optical, electrical and photoresponse properties of heterojunctions-based photodiodes. *J. Alloys Compd.* **2021**, *872*, No. 159624.

(32) Turut, A.; Karabulut, A.; Ejderha, K.; Bıyıklı, N. Capacitance−conductance characteristics of Au/Ti/Al_2O_3/n-GaAs structures with very thin Al_2O_3 interfacial layer. *Mater. Res. Express* **2015**, *2*, No. 046301.

(33) Buyukbas-Ulusan, A.; Taşçıoğlu, I.; Tataroglu, A.; Yakuphanoglu, F.; Altındal, S. A comparative study on the electrical and dielectric properties of Al/Cd-doped ZnO/p-Si structures. *J. Mater. Sci. Mater. Electron.* **2019**, *30*, 12122−12129.

(34) Sun, J.; Yang, X.; Sun, S.; Zhao, Li.; Wang, S.; Li, Y. Recent progress of rare earth conversion material in perovskite solar cells: A mini review. *Inorg. Chem. Commun.* **2022**, *143*, No. 109731.

(35) Pang, H.-S.; Xu, H.; Tang, C.; Meng, L.-K.; Ding, Y.; Xiao, J.; Liu, R.-L.; Pang, Z.-Q.; Huang, W. Capacitance methodology for investigating defect states in energy gap of organic semiconductor. *Org. Electron.* **2019**, *65*, 275−299.

(36) Méndez, M.; Palomares, E. Alq_3 (tris(8-hydroxyquinolinato)-aluminium) as a selective n-type contact for FAMAPIBr perovskite solar cells with efficient energy transfer to increase the solar cell photocurrent. *RSC Adv.* **2017**, *7*, 35525.

(37) Yerişkin, S. A.; Balbaşı, M.; Orak, I. Frequency dependent electrical characteristics and origin of anomalous capacitance-voltage (C-V) peak in Au/(Graphene-Doped PVA)/n-Si capacitors. *J. Mater. Sci. Mater. Electron.* **2017**, *28*, 7819−7826.

(38) Aslan, F.; Esen, H.; Yakuphanoglu, F. Electrical and fotoconducting characterization of Al/coumarin:ZnO/Al novel organic-inorganic hybrid photodiodes. *J. Alloys Compd.* **2019**, *789*, 595−606.

(39) Güllü, Ö.; Türüt, A. Electrical analysis of organic dye-based MIS Schottky contacts. *Microelectron. Eng.* **2010**, *87*, 2482−2487.

(40) Çetinkaya, H. G.; Sevgili, Ö.; Altındal, Ş. The fabrication of Al/p-Si (MS) type photodiode with (%2 ZnO-doped CuO) interfacial layer by sol gel method and their electrical characteristics. *Phys. B* **2019**, *560*, 91−96.

https://doi.org/10.1021/acsomega.3c00962
ACS Omega 2023, 8, 24883−24892

(41) Ersöz Demir, G.; Yücedag, I.; Azizian-Kalandaragh, Y.; Altındal, S. Temperature and interfacial layer effects on the electrical and dielectric properties of Al/(CdS-PVA)/p-Si (MPS) structures. *J. Electron. Mater.* **2018**, *47*, 6600−6606.
(42) Khan, M. B.; Khan, Z. H. Ag-incorporated Alq_3 nanowires: promising material for organic luminescent devices. *J. Lumin.* **2017**, *188*, 418−422.
(43) Elgazzar, E.; Dayan, O.; Serbetci, Z.; Dered, A.; Al-Sehemi, A. G.; Al-Ghamdi, A. A.; El-Tantawya, F.; Farooq, W. A.; Yakuphanoglu, F. Heteroleptic neutral Ru(II) complexes based photodiodes. *Phys. B* **2017**, *516*, 7−13.
(44) Erdoğan, M.; Orhan, Z.; Das, E. Synthesis of electron-rich thiophene triphenylamine based organic material for photodiode applications. *Opt. Mater.* **2022**, *128*, No. 112446.

https://doi.org/10.1021/acsomega.3c00962
ACS Omega 2023, 8, 24883−24892